

Thermal boundary conductance of sharp metal-diamond interfaces predicted by machine learning molecular dynamics

Khalid Zobaid Adnan¹, Tianli Feng^{1*}

¹Department of Mechanical Engineering, University of Utah, Salt Lake City, Utah 84112, United States

*tianli.feng@utah.edu

Abstract:

Thermal transport across sharp metal-diamond interfaces plays a critical role in the thermal management of future diamond-based ultrawide bandgap semiconductor devices. However, experimental thermal boundary conductance (TBC) values are mostly nonexistent, and current theoretical models are inaccurate in predicting the TBCs since accurate interatomic potentials of metal-diamond heterostructures are unavailable. In this letter, we show the prediction of TBCs of several practically promising sharp metal-diamond interfaces using nonequilibrium molecular dynamics (NEMD) simulations by developing accurate machine learning interatomic potentials (MLIPs). The predicted TBCs of Al, Mo, Zr, and Au-diamond interfaces are approximately 316, 88, 52, and 55 MW/m²K, respectively, after quantum corrections. The corresponding thermal boundary resistances (TBRs) are equivalent to 0.75- μ m thick of Al, 1.38- μ m Mo, 0.30- μ m Zr and 5.28- μ m Au, respectively. These low TBC values need to be considered in future diamond-based semiconductor designs. We also find that, the conventional simple models such as the acoustic mismatch model (AMM) and diffuse mismatch model (DMM), even including the full band phonon dispersion from first principles, largely mispredict the TBC because they do not include inelastic transmission as well as interfacial structural and bonding information. The quantum correction of TBC matches well with the quantum correction of phonon specific heat of metals, instead of diamond. Additionally, we reveal that the Debye temperature ratio is a better indicator of TBC than the elastic modulus ratio.

Diamond has an ultra-wideband gap¹ (5.5 eV), high carrier mobility^{2,3}, large breakdown field⁴ (>10 MV/cm), low thermal expansion^{5,6} and the highest thermal conductivity^{7–10} (2200 W/m-K) in nature, which makes it an ideal future material for extreme semiconductors for next-generation power devices^{11–13}. High electron mobility transistors (HEMT)^{14,15} result in significant self-heating of devices. As the channel material, the diamond must be integrated with the metal electrodes¹⁶. In addition to the traditional heat dissipation downward through the diamond and substrate, an additional pathway upward through the metal electrodes could significantly enhance the thermal management of diamond-based power electronics¹⁷. The thermal boundary resistance (TBR), which is reciprocal of TBC, at metal-diamond interfaces can contribute substantial thermal

resistance in these devices. Gaining a comprehensive understanding of heat transfer at the clean metal-diamond interfaces is vital not only for ensuring the reliability and performance of diamond-based power devices but also for playing a key role in the broader context of thermal management¹⁸. Moreover, the interfaces between metals and semiconductors are a common feature not just in electrodes but also in devices like junction field-effect transistors¹⁹ and Schottky barrier diodes²⁰⁻²², offering valuable insights and opportunities for the design and performance optimization of semiconductor devices.

TBCs of various metal-diamond interfaces have been measured in recent years. In Al-diamond interfaces, time domain thermoreflectance (TDTR) experimental values reported are widely spread across a range of 25-250 MW/m²K for different surface treatments and orientations of diamond in Monachon *et al.*^{23,24}. They attributed these values to being associated with different surface treatments of the substrate before depositing Al. Mo-diamond interface has a TBC of approximately about 60-285 MW/m²K reported by Monachon *et al.*²⁵. However, the interface includes a carbide formation (MoC₂), thereby impacting the TBC across the interface. In another study, Monachon *et al.*²⁶ predicted the TBC to be around 220-240 with a partial carbide formation of unknown Mo/Mo_xC_y at the interface. TBC of Au-diamond interface from experimental data of Hohensee *et al.*²⁷ suggest TBC values in the range of approximately 134 MW/m²K, observed at a pressure of about 34-35 GPa. It is worth noting that TBC at metal-diamond interfaces is influenced by pressure, as it has the potential to enhance interfacial bonding. The influence of nanometer-thick interlayers, utilizing either nickel or molybdenum, were also investigated²⁸. The reported TBC without any interlayer, was approximately 76 MW/m²K²⁸. The TBC of Au-diamond interfaces was reported to be about 40 MW/m²K by Stoner *et al.*²⁹. However, these experimental measurements were based on metal-diamond interfaces with various oxides, surface treatments and carbide formations, altering the interfacial atomic structure. The intrinsic TBCs of sharp metal-diamond interfaces, which are the designs of future diamond-based ultra-wide bandgap semiconductor devices, are unclear.

Alongside experimental investigations, numerous theoretical studies have been undertaken to comprehend and predict the TBCs of metal-diamond interfaces. Lombard *et al.* reported a TBC of 130 MW/m²K for an Al-diamond interface using DMM³⁰. In contrast, the reported values for TBC from DMM were 365 MW/m²K by Battyabal *et al.*³¹. Additionally, their work included the modified scattering-mediated acoustic mismatch model (SMAMM), which predicted a TBC of 225 MW/m²K. Similarly, the TBC of Au-diamond interfaces has been predicted to be around 13 MW/m²K from DMM³⁰.

However, the theoretical models have their limitations. The models frequently oversimplify phonon transmission by neglecting inelastic contributions and may disregard bonding information between dissimilar materials. Most of these models rely on the evaluation of phonon transmission coefficients at the interfaces. To calculate phonon transmission coefficients, common ways are acoustic mismatch (AMM)³², diffuse mismatch (DMM)^{33,34}, and atomistic Green's function (AGF)

^{35–38}. The limitation of AMM and DMM is that they neglect the inelastic transmission and ignore the detailed atomic structure and bonding strength at the interface. The limitation of harmonic atomistic Green's function (AGF) is that it ignores inelastic transmission, and the limitation of the very recently developed anharmonic AGF is its extreme computational cost for complex interfaces with interlayer structures. Despite the improvement made by some works^{39–47}, they ignore some critical phenomena, such as the existence of interfacial phonon modes and the local phonon nonequilibrium⁴⁸. The wave-packet method^{49–53} is an effective way to study phonon transmission, but it usually studies one mode at a time, which is time-consuming. More importantly, it is typically performed at 0 K, assuming all the other modes are frozen out, which misses the phonon-phonon coupling effect at finite temperatures. Compared to the above-mentioned methods based on phonon transmission coefficients, MD can naturally include all the physical phenomena near the interfaces⁴⁸, and many spectral phonon analysis methods have been developed to gain insights of phonon transport in MD^{48,54–62}. But MD severely depends on interatomic potentials, which are nonexistent for most heterostructures (and not accurate if they exist).

In this letter, we develop accurate MLIPs based on ab initio molecular dynamics (AIMD) simulation trajectories, and then conduct NEMD simulations to predict the TBCs. MLIPs trained from AIMD can ensure both the accuracy and computational efficiency of the NEMD simulations. The systems studied in this work include Al, Zr, Mo, and Au-diamond interfaces, as shown in Fig. 1. Quantum corrections are done to incorporate the quantum effects. The results are compared to the measured data in the literature. DMM (Full band)⁶³, DMM (Debye), AMM and AMM (Debye) calculations are evaluated to serve as a comparison.

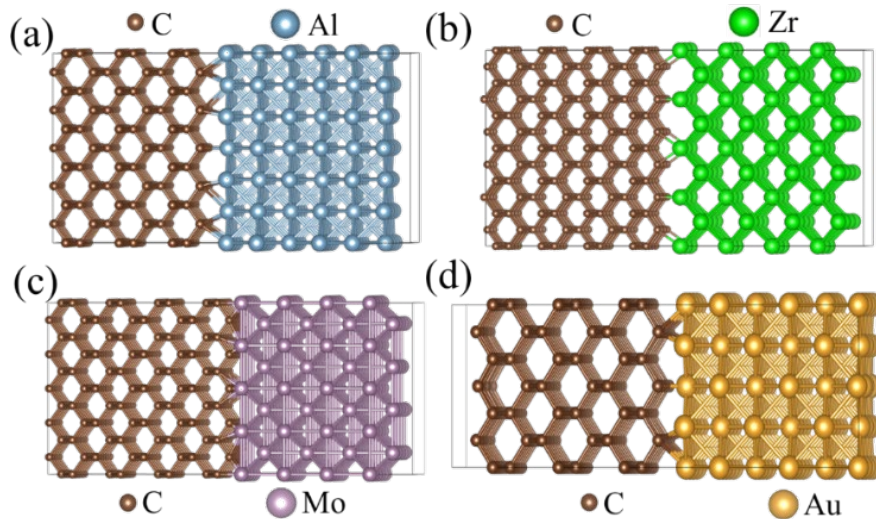


FIG. 1. Four representative interfacial structures of metal-diamond interfaces with atom labels in (a) Al-diamond, (b) Zr-diamond (c) Mo-diamond (d) Au-diamond interface.

It is challenging to construct metal-diamond heterostructures in AIMD simulations since metals and diamond have large lattice mismatch. To make sure heterostructures are most realistic and at the same with manageable computational cost, the heterostructures are chosen as $5 \times 5 \times 3$ (Al) and $3 \times 3 \times 3$ (diamond), $4 \times 4 \times 3$ (Zr) and $2 \times 2 \times 3$ (diamond), $4 \times 4 \times 4$ (Mo) and $5 \times 5 \times 4$ (diamond), and $4 \times 4 \times 4$ (Au) and $3 \times 3 \times 3$ (diamond), respectively, as shown in Fig. 1. The lattice mismatch will induce pressure laterally and induce strains on the metal side. The strain on diamond is negligible as it has a much larger modulus than metals. We first try to relax the lattice along the heat transport (axial) direction so that there is no stress along the axial direction, but we find that this will induce phase change to the metals since the lateral directions have large stress. To preserve the metals' crystal symmetries, we let the strain along the axial direction the same as the lateral directions. In the final structures, Al, Zr, Mo, and Au-diamond heterostructures have isotropic pressures of 5-6 GPa, 4.5-5 GPa, 0.7-0.8 GPa, and 34-35 GPa, respectively. We understand that these pressures will overestimate the TBCs of sharp interfaces. Therefore, this study will serve as an upper limit of TBCs of these interfaces.

The AIMD simulations are conducted by using the Vienna Ab initio Simulation Package^{64,65} (VASP) with the projector augmented wave (PAW)⁶⁶ Perdew-Burke-Ernzerhof (PBE)⁶⁷ pseudopotentials. The energies, stresses, atomic forces, and atomic configurations in the AIMD simulations are used to train the moment-tensor machine learning potentials (MTPs) by using the MLIP package⁶⁸. The energy cutoffs are set to be 450 eV. Γ point, only electronic \mathbf{k} -mesh is used. For each interface, we run 2 - 6 independent AIMD simulations, each containing 1,000 - 1,500 steps at 300 K. Each simulation starts with random atomic positions, which are perturbed slightly to the crystallized structures, and velocities. The timestep is 1 fs. The output files generated from AIMD contain energy, forces, and stresses for each timestep, which are used for MLIP training. The minimum and maximum cutoff radii of the MLIP are set at 1.0 and 6.0, 0.9 and 3.8, 0.96 and 5.0, and 0.92 and 3.8 Å for Al, Zr, Mo, and Au-diamond interfaces, respectively. The training level⁶⁸ is set as 24. The number of iterations for training is set to 500. 80-90% of the data is allocated for the training, and the remaining portion is designated for the testing. The accuracy of the MLIPs is demonstrated in Fig. 2. Generally, the forces predicted by the MLIP agree very well with those predicted directly from AIMD for all four structures.

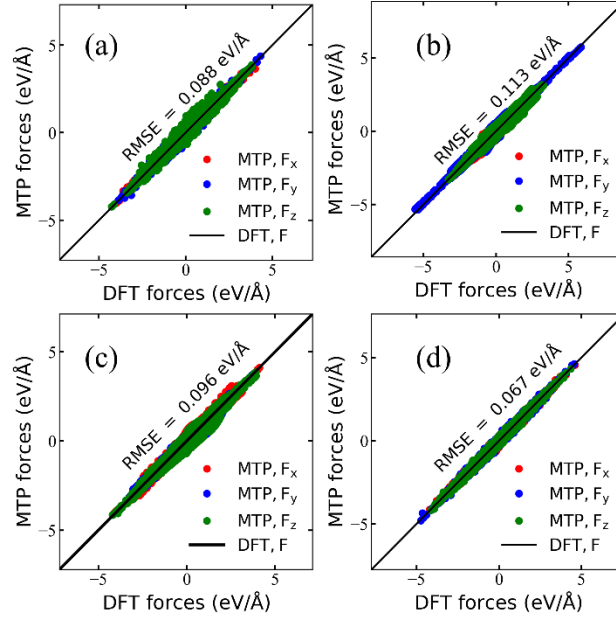


FIG 2: Comparisons of forces on atoms between MTP and DFT calculations for (a) Al-diamond, (b) Zr-diamond, (c) Mo-diamond, and (d) Au-diamond. The RMSE is evaluated by directly comparing data between MTP and DFT calculations.

With the trained MTPs, we run NEMD simulations using the Large-scale Atomic/Molecular Massively Parallel Simulator (LAMMPS)⁶⁹. The atoms at the two edges are fixed to mimic the adiabatic boundary condition. The systems are first stabilized in NVT at 300 K for 3 million steps with a timestep of 1 fs. Then, the metal atoms next to the fixed boundary are changed to 320 K as the hot reservoir, and the diamond atoms next to the fixed boundary are changed to 280 K as the cold reservoir, both using the Langevin thermostat⁷⁰. The number of atoms in both reservoirs is approximately 200. Then, the ensemble is changed to NVE and runs for another 2 million steps. After that, the temperature and heat flux are recorded for another 2 million steps. The TBC is calculated by using $G = \frac{q}{A \cdot \Delta T}$, where q is the heat flux, ΔT is the temperature jump at the interface, and A is the cross-section area.

The TBCs predicted by machine learning molecular dynamics (MLMD) after quantum correction are shown in Fig. 3, compared to the available experimental data. The predicted TBC values are 316 ± 22 , 88 ± 8 , 51 ± 8 , and 55 ± 5 for Al, Mo, Zr and Au-diamond interfaces, respectively. The corresponding thermal boundary resistances (TBRs) are equivalent to 0.75- μm thick of Al, 1.38- μm Mo, 0.30- μm Zr and 5.28- μm Au, respectively. They are not too small to be neglected in real devices since most thickness of metal electrodes in wide bandgap semiconductor transistors are in

nano to micrometer scale^{71–74}. Note that, in our MLMD simulations, pressure exists, and the TBC values with zero pressure should be even lower than the reported values here.

It is observed that the Al-diamond interface has the highest TBC value, followed by the Mo-diamond, Zr-diamond, and Au-diamond interfaces. The Al-diamond interface exhibits the least vibrational mismatch compared to the other interfaces. This dominance of vibrational match contributes to its higher thermal boundary conductance (TBC) compared to the other interfaces. The exception occurs between the Mo and Zr-diamond interfaces. Despite that the Zr-diamond exhibits a smaller mass mismatch^{75,76}, it shows a lower TBC. This is because the Zr-diamond interface has a larger phonon mismatch than the Mo-diamond interface, which will be discussed later.

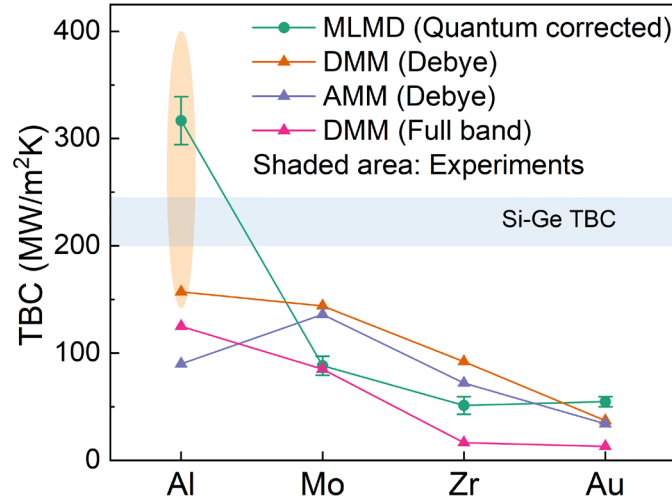


FIG 3: TBC of Al, Zr, Mo, and Au-diamond interfaces from MLMD (quantum corrected), AMM (Debye), DMM (Debye), and DMM (Full band) models. Isotropic pressures of 5-6, 4.5-5, 0.7-0.8, and 34-35 GPa exist in the MLMD simulations, respectively. Yellow shaded indicates the TBC measured for Al-diamond interface by Hohensee *et al.*²⁷ from 0 to 50 GPa. Blue shaded area represents the TBC of sharp and interfacial mixing Si-Ge interface⁷⁷.

For the Al-diamond interface, the TBC values measured from the time domain thermoreflectance (TDTR) are widely spread across a range of 21-390 MW/m²K^{23,24,27,78}. It depends primarily on the surface termination of the substrate before depositing Al. Monachen *et al.* found that surface treatments and Al deposition techniques can also affect the TBC value^{23,24}, due to the change of cleanliness and surface termination of diamond. The hydrogen-treated diamond surfaces exhibit a TBC four times lower than that of oxygenated diamond interfaces, as reported by Collins *et al.*⁷⁸. The surface termination dependence is reported due to differences in carrier scattering in the Al near the interfacial region. Hohensee *et al.*²⁷ measured that TBC can increase with pressure in a

range of 150 - 400 MW/m²K for 0-40 GPa. Our MLMD results reveal TBC of approximately 316 ± 22 MW/m²K at an average pressure about 5-6 GPa, which is slightly above the upper limit of the TBC data of 180-280 MW/m²K measured by Hohensee *et al.*²⁷ in the same pressure range. The slightly higher MLMD result could be attributed to the perfect purity of the interface, with no impurities, doping, or vacancies present in the simulated structure of the Al-diamond interface. Interestingly, the Al-diamond TBC values are similar to and even higher than that of clean Si-Ge interface, which is about 200-240 MW/m²K⁷⁷. Compared to Al-diamond, Si-Ge has a much better lattice match, phonon vibrational match, and chemical bonding at the interface. It is still an open question why Al-diamond can have higher TBC than Si-Ge.

For the Mo-diamond interface, the predicted TBC of 88 ± 8 MW/m²K is significantly smaller than the measured value of 220 -240 MW/m²K. This is because the measured data was based on Mo-Mo_xC_y interface rather than a sharp Mo-diamond interface⁷⁹. The Mo_xC_y (Mo/diamond composite) might contribute to a bridging effect^{80,81}, which can enhance TBC. Unfortunately, there is no experimental TBC data available for the sharp Mo-diamond interface. Regarding the Zr-diamond interface, there is no experimental data available, either.

For the Au-diamond interface, the experimental TBC from Hohensee *et al.*²⁷ is about 130 MW/m²K, observed at a pressure of about 30-35 GPa. It is much higher than the 55 ± 5 MW/m²K obtained in MLMD simulations at a similar pressure of 34-36 GPa. This might be because of two reasons: the experiment data was measured for Au (Pd)-diamond interface, an alloy like structure, rather than Au-diamond interface; the surface treatment of diamond increases the adhesion forces and TBC. Without pressure²⁷, the TBC was measured to be about 70 MW/m²K, which is very close to the data, 76 MW/m²K, measured by Blank *et al.*²⁸. The insertion of a nanometer-thick Ni or Mo interlayer increases TBC to 195 ± 40 MW/m²K²⁸ due to bridging effect^{80,81}. In another report by Stoner *et al.*²⁹, the TBC of Au-diamond interfaces was measured to be about 40 MW/m²K, but detailed interfacial structure information is missing. In summary, the sharp Au-diamond interface TBC might be much smaller than 55 MW/m²K and adding interfacial mixing or interlayer can largely increase it.

The interfaces between diamond and the other metals such as Cu, Pt, Pb, Nb, and W have also been extensively studied experimentally. They show a similar TBC range as the four metal interfaces we study in this work. For example, the TBC of Cu-diamond interface is about 33-73 MW/m²K⁸² and can be enhanced to 96 MW/m²K with a Cr interlayer⁸³ and 87 MW/m²K with a Mo interlayer⁸⁴. The TBC of Pt-diamond interface increases from 145 to 240 MW/m²K with pressure increasing from 0 to 50 GPa. The TBC of Pb-diamond interface increases from 30 to 140 MW/m²K from 0 to 50 GPa²⁷. The TBC of Nb-diamond interface is about 70 MW/m²K, possibly with some carbide formation⁸⁵. The TBC of W-diamond interfaces exhibit a wide range of 40 - 190 MW/m²K.

The MLMD provides much more accurate predictions, compared to the conventional AMM and DMM based models. To make a comparison, we calculate the TBCs using DMM and AMM under

the Debye approximation, as well as the DMM with the exact full band phonon dispersion from first principles. Under the Debye model, the thermal conductance G based on Landauer's formalism⁸⁶ is.

$$G_{\text{Debye}} = \frac{1}{4} \sum_j v_{A,j} \int_0^{\omega_{D,A}} \alpha_{A \rightarrow B} \hbar \omega \frac{df_{A,j}}{dT} d\omega, \quad (1)$$

$$f_{A,j}(\omega, T) = \frac{\omega^2}{2\pi^2 v_{A,j}^3 [\exp(\frac{\hbar\omega}{k_B T}) - 1]}, \quad (2)$$

where $v_{A,j}$ is the sound velocity of material A in the polarization branch j , $\omega_{D,A}$ is the Debye frequency of material A calculated by $\omega_{D,A} = v_{A,j} (6\pi^2 n_A)^{\frac{1}{3}}$ with n_A being the number density of atoms in A, $\alpha_{A \rightarrow B}$ is the phonon transmission coefficient from A to B, \hbar is the reduced Planck constant, ω is the phonon angular frequency, $f_{A,j}$ is the phonon population under Debye approximation, and k_B is the Boltzmann constant. $\alpha_{A \rightarrow B}$ can be obtained from AMM (assuming normal incident of phonons) and DMM using the following equations:

$$\alpha_{A \rightarrow B, \text{AMM}} = \frac{4Z_A Z_B}{(Z_A + Z_B)^2}, \quad (3)$$

$$\alpha_{A \rightarrow B, \text{DMM}} = \frac{\sum_j v_{B,j}^{-2}}{\sum_j v_{B,j}^{-2} + \sum_j v_{A,j}^{-2}}. \quad (4)$$

Here, Z_A and Z_B are acoustic impedances of materials A and B, respectively. For DMM, we also conduct full-band Landauer's formalism^{63,87,88} calculation by

$$G_{\text{DMM,full}} = \frac{1}{2(2\pi)^3} \sum_{j_A} \int_{\text{BZ}_A} c_{\lambda_A} \alpha_{A \rightarrow B}(\omega_{\lambda_A}) |v_{\lambda_A, n}| d\mathbf{q}_A = \frac{1}{2N_{\mathbf{q},A} V_{c,A}} \sum_{j_A} \sum_{\mathbf{q}_A} c_{\lambda_A} \alpha_{A \rightarrow B}(\omega_{\lambda_A}) |v_{\lambda_A, n}| \quad (5)$$

$$\alpha_{A \rightarrow B}(\omega) = \frac{\Delta \mathbf{q}_B \cdot (\sum_{\lambda_B} |v_{\lambda_B, n}| \cdot \delta_{\omega_{\lambda_B}, \omega})}{\Delta \mathbf{q}_A \cdot (\sum_{\lambda_A} |v_{\lambda_A, n}| \cdot \delta_{\omega_{\lambda_A}, \omega}) + \Delta \mathbf{q}_B \cdot (\sum_{\lambda_B} |v_{\lambda_B, n}| \cdot \delta_{\omega_{\lambda_B}, \omega})}. \quad (6)$$

Here, $c_{\lambda_A} = k_B x^2 \frac{e^x}{(e^x - 1)^2}$ is the specific heat of A per mode, $x = \frac{\hbar \omega_{A, \lambda}}{k_B T}$, $v_{A, \lambda, n} = |\mathbf{v}_{A, \lambda} \cdot \mathbf{n}|$, \mathbf{n} is the unit vector normal to the interface, \mathbf{q}_A is the wavevector of material A, $\lambda_A \equiv (\mathbf{q}_A, j_A)$ is the phonon mode in A with wavevector \mathbf{q}_A and branch j_A , $\lambda_B \equiv (\mathbf{q}_B, j_B)$ is the phonon mode in B, and $\Delta \mathbf{q}_A = \frac{V_{A, \text{BZ}}}{N_{\mathbf{q},A}}$ and $\Delta \mathbf{q}_B = \frac{V_{B, \text{BZ}}}{N_{\mathbf{q},B}}$ are the discretized Brillouin zone volume in material A and B, respectively. $V_{A, \text{BZ}}$ is the volume of the Brillouin zone of A, $N_{\mathbf{q},A}$ is the number of \mathbf{q} points sampled in A, and $V_{c,A}$ is the primitive cell volume of A. Same for B.

The results of AMM and DMM models' calculations are shown in Fig. 3. It is found that all the AMM, DMM, and DMM (Full band) predictions are inaccurate and not reliable, compared to MLMD. DMM (full band) usually significantly underestimates the TBCs, as it does not consider inelastic phonon transmissions⁸⁹. Additionally, the AMM and DMM models do not account for the strength of atomic bonding or interfacial atomistic structure at the interface.

The limitation of MLMD is its classical nature of MD, which should be quantumly corrected. In order to have a sense on the quantum correction of TBC, we plotted the TBC_Q/TBC_C predicted from DMM (full band), where the subscript “Q” means the phonon specific heat is quantum in Eq. (5), i.e., $c = k_B \chi^2 \frac{e^x}{(e^x - 1)^2}$, and the subscript “C” means the phonon specific heat is classical in Eq. (5), i.e., $c = k_B$. As shown in Fig 4 (a), the ratio of TBC_Q/TBC_C follows very well with the ratio of phonon specific heat $c_{ph,Q}/c_{ph,C}$ of the four metals. Obviously, TBC_Q/TBC_C does not follow the ratio of phonon specific heat $c_{ph,Q}/c_{ph,C}$ of diamond, which has a high Debye temperature of 2200 K. The reason is that in the DMM model, all transmission is elastic, and only the phonons below the cutoff frequency of the lower side, which is metal for metal-diamond interface can contribute to the interfacial conductance. Therefore, at the first-order approximation, we use c_Q/c_C as the quantum correction of the obtained TBC from MLMD, i.e., $G_{MLMD,Q} = G_{MLMD,C} \cdot \frac{c_{ph,Q,metal}(T)}{c_{ph,C,metal}}$. All the TBC values obtained from MLMD in this paper are after quantum corrections. As shown in Fig. 4, the quantum correction of TBC at 300 K is very small since the phonon specific heat of metals at 300 K is very close to the classical limit as the Debye temperatures of these metals are close to or smaller than 300 K.

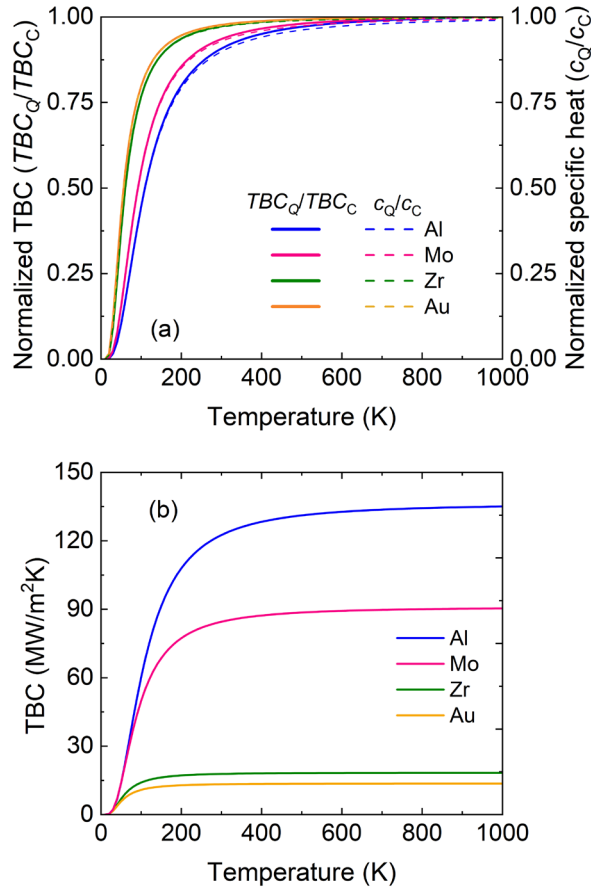


FIG 4: Results from DMM (Full band) (a) Effect of temperature on the TBC of Al, Zr, Mo, Au-diamond interfaces. The classical TBC calculations imply the specific heat to be k_B , Boltzmann constant. The normalized specific heat (C_Q/C_C) is determined by taking the ratio of the metal's quantum specific heat and its classical specific heat. Normalized TBC depicts the normalized value at any given temperature with respect to classical TBC.

To find a correlation between TBC and the metal properties for metal-diamond interfacial TBC, we plot TBC with respect to atomic mass ratio, sound velocity ratio, Young's modulus ratio, and Debye temperature ratio, as shown in Fig. 5. Typically, the TBC should reach maximum when these ratios approach 1, which indicates that the two materials are the same and the interface has the least abruptness. In Fig. 5 (a), we find that TBC increases with increasing mass match between metal and diamond, except for the order of Mo and Zr. This is because although Zr has a lighter mass and better mass match with diamond than Mo does, Zr has a softer bonding and larger bonding mismatch with diamond than Mo does. Therefore, the TBC is not only determined by mass match but also bonding match. As a result, it is determined by the Debye temperature match, which includes both mass and bonding matches, as seen in Fig. 5 (d). In comparison, sound velocity and Young's modulus are as good as Debye temperature, in terms of representing the phonon spectra match. Inspired by the results, we plot the available TBC values of various interfaces collected from the literature as functions of elastic modulus ratio and Debye temperature ratio, as shown in Fig. 6. It is noted that the Debye temperature ratio is a better descriptor of the TBC than elastic modulus ratio used in the literature^{27,77,90}. We recommend using Debye temperature ratio, rather than elastic modulus ratio, as the indicator of TBC in the future.

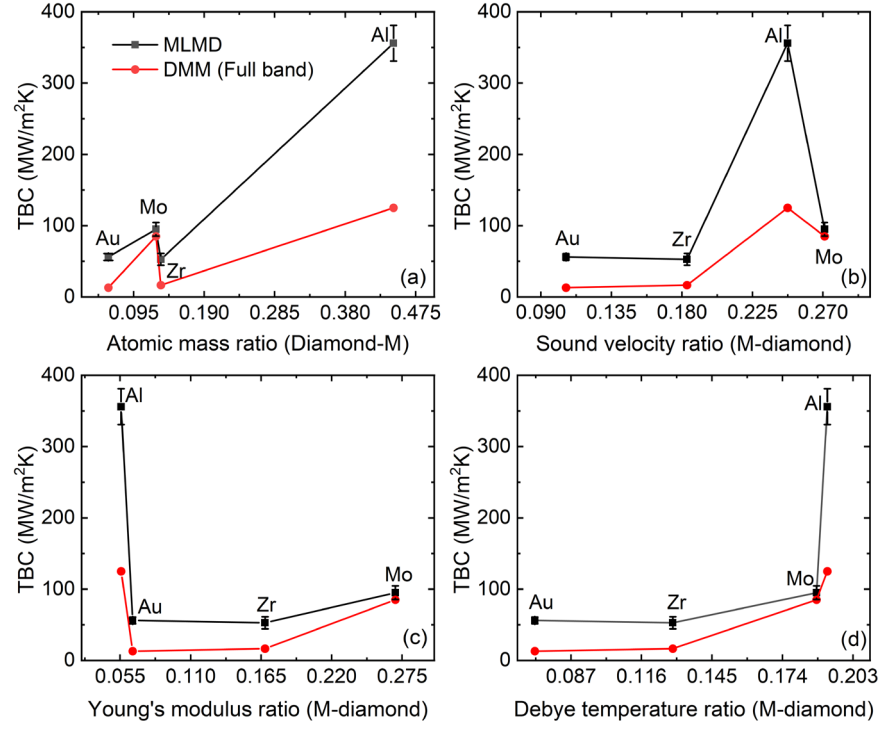


FIG 5: TBCs at different metal-diamond interfaces as a function of (a) atomic mass ratio of Diamond-M (b) sound velocity ratio of M-diamond (c) Young's modulus ratio of M-diamond and (d) Debye temperature ratio of M-diamond.

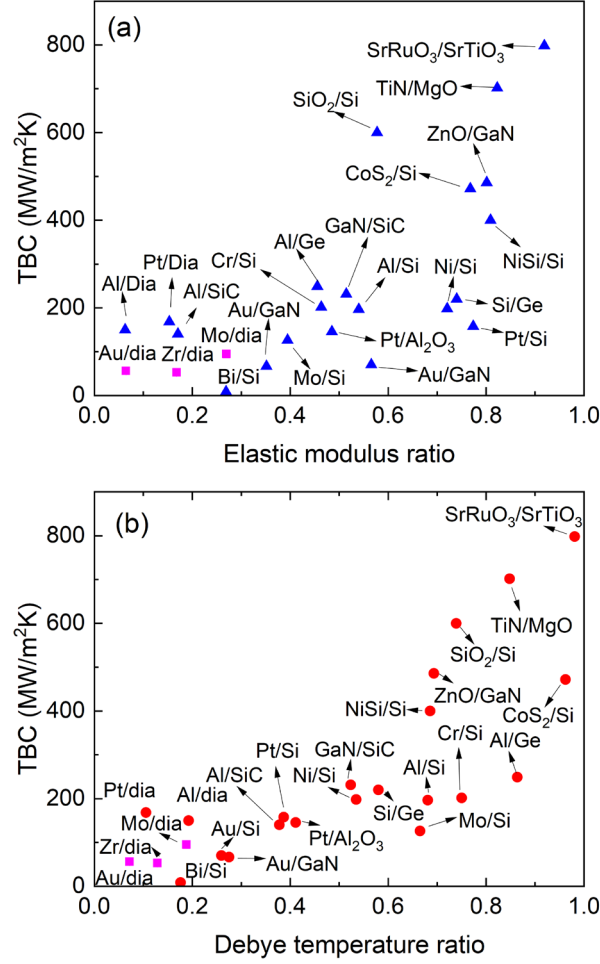


FIG 6: TBCs for various interfaces collected from the literature^{27,90} as a function of (a) elastic modulus ratio (b) Debye temperature ratio. For Mo, Zr, and Au-diamond interfaces, which do not have available experimental data, the MLMD data are shown instead.

In conclusion, we have demonstrated the predictive capabilities of machine learning interatomic potential (MLIP) in predicting thermal boundary conductance (TBC) at Al, Zr, Mo, Au-diamond interfaces. Compared to the conventional AMM and DMM model, which only consider the elastic transmission, the MLMD simulations take into account both elastic and inelastic transmission, the detailed interfacial bonding strength and structure, and all the other natural phonon transport mechanisms at the interfaces. The accuracy of MLIP is promising as indicated by low RMSE values for forces among atoms. We find that Al has the largest and Zr has the lowest TBCs, indicating a great potential of using Al as the metal electrode for diamond devices. These findings provide valuable guidance for future experimental endeavors in various metal-diamond interfaces.

This work is supported by the National Science Foundation (NSF) (award number: CBET 2337749). The support and resources from the Center for High Performance Computing at the University of Utah are gratefully acknowledged.

References:

- ¹ M.H. Wong, O. Bierwagen, R.J. Kaplar, and H. Umezawa, “Ultrawide-bandgap semiconductors: An overview,” *Journal of Materials Research* 2021 36:23 36(23), 4601–4615 (2021).
- ² J. Isberg, J. Hammersberg, E. Johansson, T. Wikström, D.J. Twitchen, A.J. Whitehead, S.E. Coe, and G.A. Scarsbrook, “High carrier mobility in single-crystal plasma-deposited diamond,” *Science* 297(5587), 1670–1672 (2002).
- ³ J. Liu, H. Yu, S. Shao, J. Tu, X. Zhu, X. Yuan, J. Wei, L. Chen, H. Ye, and C. Li, “Carrier mobility enhancement on the H-terminated diamond surface,” *Diam Relat Mater* 104, 107750 (2020).
- ⁴ H. Umezawa, “Recent advances in diamond power semiconductor devices,” *Mater Sci Semicond Process* 78, 147–156 (2018).
- ⁵ P. Jacobson, and S. Stoupin, “Thermal expansion coefficient of diamond in a wide temperature range,” *Diam Relat Mater* 97, 107469 (2019).
- ⁶ S. Stoupin, and Y. V. Shvyd’ko, “Thermal expansion of diamond at low temperatures,” *Phys Rev Lett* 104(8), 085901 (2010).
- ⁷ P.A. Loginov, D.A. Sidorenko, A.S. Orekhov, and E.A. Levashov, “A novel method for in situ TEM measurements of adhesion at the diamond–metal interface,” *Scientific Reports* 2021 11:1 11(1), 1–10 (2021).
- ⁸ G.T. Hohensee, R.B. Wilson, and D.G. Cahill, “Thermal conductance of metal–diamond interfaces at high pressure,” *Nat Commun* 6(1), 6578 (2015).
- ⁹ B. Lee, J.S. Lee, S.U. Kim, K. Kim, O. Kwon, S. Lee, J.H. Kim, and D.S. Lim, “Simultaneous measurement of thermal conductivity and interface thermal conductance of diamond thin film,” *Journal of Vacuum Science & Technology B: Microelectronics and Nanometer Structures* 27(6), 2408 (2009).

- ¹⁰ A. V. Inyushkin, “Thermal conductivity of group IV elemental semiconductors,” *J Appl Phys* 134(22), 221102 (2023).
- ¹¹ G. Perez, A. Maréchal, G. Chicot, P. Lefranc, P.O. Jeannin, D. Eon, and N. Rouger, “Diamond semiconductor performances in power electronics applications,” *Diam Relat Mater* 110, 108154 (2020).
- ¹² P.J. Wellmann, “Power Electronic Semiconductor Materials for Automotive and Energy Saving Applications – SiC, GaN, Ga₂O₃, and Diamond,” *Z Anorg Allg Chem* 643(21), 1312–1322 (2017).
- ¹³ N. Donato, N. Rouger, J. Pernot, G. Longobardi, and F. Udrea, “Diamond power devices: state of the art, modelling, figures of merit and future perspective,” *J Phys D Appl Phys* 53(9), 093001 (2019).
- ¹⁴ Y. Zhou, J. Anaya, J. Pomeroy, H. Sun, X. Gu, A. Xie, E. Beam, M. Becker, T.A. Grotjohn, C. Lee, and M. Kuball, “Barrier-layer optimization for enhanced GaN-on-diamond device cooling,” *ACS Appl Mater Interfaces* 9(39), 34416–34422 (2017).
- ¹⁵ H. Guo, Y. Kong, and T. Chen, “Thermal simulation of high power GaN-on-diamond substrates for HEMT applications,” *Diam Relat Mater* 73, 260–266 (2017).
- ¹⁶ S.P. Gimenez, “Diamond MOSFET: An innovative layout to improve performance of ICs,” *Solid State Electron* 54(12), 1690–1696 (2010).
- ¹⁷ K. Yoshida, and H. Morigami, “Thermal properties of diamond/copper composite material,” *Microelectronics Reliability* 44(2), 303–308 (2004).
- ¹⁸ N. Govindaraju, and R.N. Singh, “Processing of nanocrystalline diamond thin films for thermal management of wide-bandgap semiconductor power electronics,” *Materials Science and Engineering: B* 176(14), 1058–1072 (2011).
- ¹⁹ K. Tsugawa, H. Umezawa, and H. Kawarada, “Characterization of diamond surface-channel metal-semiconductor field-effect transistor with device simulation,” *Japanese Journal of Applied Physics, Part 1: Regular Papers and Short Notes and Review Papers* 40(5 A), 3101–3107 (2001).
- ²⁰ M. Suzuki, S. Koizumi, M. Katagiri, T. Ono, N. Sakuma, H. Yoshida, T. Sakai, and S. Uchikoga, “Electrical characteristics of n-type diamond Schottky diodes and metal/diamond interfaces,” *Physica Status Solidi (a)* 203(12), 3128–3135 (2006).
- ²¹ C. Cheng, Z. Zhang, X. Sun, Q. Gui, G. Wu, F. Dong, D. Zhang, Y. Guo, and S. Liu, “Ab-initio study of Schottky barrier heights at metal-diamond (1 1 1) interfaces,” *Appl Surf Sci* 615, 156329 (2023).
- ²² P.K. Baumann, S.P. Bozeman, B.L. Ward, and R.J. Nemanich, “Characterization of metal-diamond interfaces: Electron affinity and Schottky barrier height,” *Diam Relat Mater* 6(2–4), 398–402 (1997).
- ²³ C. Monachon, and L. Weber, “Effect of diamond surface orientation on the thermal boundary conductance between diamond and aluminum,” *Diam Relat Mater* 39, 8–13 (2013).
- ²⁴ C. Monachon, and L. Weber, “Influence of diamond surface termination on thermal boundary conductance between Al and diamond,” *J Appl Phys* 113(18), 183504 (2013).

- ²⁵ C. Monachon, and L. Weber, "Thermal boundary conductance of transition metals on diamond," *Emerging Materials Research* 1(2), 89–98 (2012).
- ²⁶ C. Monachon, and L. Weber, "Thermal boundary conductance between refractory metal carbides and diamond," *Acta Mater* 73, 337–346 (2014).
- ²⁷ G.T. Hohensee, R.B. Wilson, and D.G. Cahill, "Thermal conductance of metal–diamond interfaces at high pressure," *Nature Communications* 2015 6:1 6(1), 1–9 (2015).
- ²⁸ M. Blank, G. Schneider, J. Ordóñez-Miranda, and L. Weber, "Role of the electron-phonon coupling on the thermal boundary conductance of metal/diamond interfaces with nanometric interlayers," *J Appl Phys* 126(16), (2019).
- ²⁹ R.J. Stoner, and H.J. Maris, "Kapitza conductance and heat flow between solids at temperatures from 50 to 300 K," *Phys Rev B* 48(22), 16373 (1993).
- ³⁰ J. Lombard, F. Detcheverry, and S. Merabia, "Influence of the electron–phonon interfacial conductance on the thermal transport at metal/dielectric interfaces," *Journal of Physics: Condensed Matter* 27(1), 015007 (2014).
- ³¹ M. Battabyal, O. Beffort, S. Kleiner, S. Vaucher, and L. Rohr, "Heat transport across the metal–diamond interface," *Diam Relat Mater* 17(7–10), 1438–1442 (2008).
- ³² W.A. Little, "THE TRANSPORT OF HEAT BETWEEN DISSIMILAR SOLIDS AT LOW TEMPERATURES," *Can J Phys* 37(3), 334–349 (1959).
- ³³ E.T. Swartz, and R.O. Pohl, "Thermal resistance at interfaces," *Appl Phys Lett* 51(26), 2200–2202 (1987).
- ³⁴ E. Swartz, and R. Pohl, "Thermal boundary resistance," *Rev Mod Phys* 61(3), 605–668 (1989).
- ³⁵ W. Zhang, N. Mingo, and T. Fisher, "Simulation of phonon transport across a non-polar nanowire junction using an atomistic Green's function method," *Phys Rev B* 76(19), 195429 (2007).
- ³⁶ W. Zhang, T.S. Fisher, and N. Mingo, "Simulation of Interfacial Phonon Transport in Si–Ge Heterostructures Using an Atomistic Green's Function Method," *J Heat Transfer* 129(4), 483 (2007).
- ³⁷ N. Mingo, and L. Yang, "Phonon transport in nanowires coated with an amorphous material: An atomistic Green's function approach," *Phys Rev B* 68(24), 245406 (2003).
- ³⁸ Z. Tian, K. Esfarjani, and G. Chen, "Enhancing phonon transmission across a Si/Ge interface by atomic roughness: First-principles study with the Green's function method," *Phys Rev B* 86(23), 235304 (2012).
- ³⁹ P.E. Hopkins, and P.M. Norris, "Effects of joint vibrational states on thermal boundary conductance," *Nanoscale and Microscale Thermophysical Engineering* 11(3–4), 247–257 (2007).
- ⁴⁰ P.E. Hopkins, and P.M. Norris, "Relative contributions of inelastic and elastic diffuse phonon scattering to thermal boundary conductance across solid interfaces," *J Heat Transfer* 131(2), 022402 (2009).

- ⁴¹ P.E. Hopkins, J.C. Duda, and P.M. Norris, “Anharmonic phonon interactions at interfaces and contributions to thermal boundary conductance,” *J Heat Transfer* 133(6), 062401 (2011).
- ⁴² R. Prasher, X. Hu, Y. Chalopin, N. Mingo, K. Lofgreen, S. Volz, F. Cleri, and P. Keblinski, “Turning Carbon Nanotubes from Exceptional Heat Conductors into Insulators,” *Phys Rev Lett* 102(10), 105901 (2009).
- ⁴³ P. Reddy, K. Castelino, and A. Majumdar, “Diffuse mismatch model of thermal boundary conductance using exact phonon dispersion,” *Appl Phys Lett* 87(21), 1–3 (2005).
- ⁴⁴ S. Sadasivam, N. Ye, J.P. Feser, J. Charles, K. Miao, T. Kubis, and T.S. Fisher, “Thermal transport across metal silicide-silicon interfaces: First-principles calculations and Green’s function transport simulations,” *Phys Rev B* 95(8), 085310 (2017).
- ⁴⁵ S. Volz, editor, *Thermal.Nanosystems.and.Nanomaterials* (Springer Berlin Heidelberg, Berlin, Heidelberg, 2009).
- ⁴⁶ S. Shin, M. Kaviani, T. Desai, and R. Bonner, “Roles of atomic restructuring in interfacial phonon transport,” *Phys Rev B* 82(8), 081302 (2010).
- ⁴⁷ J. Dai, and Z. Tian, “Rigorous formalism of anharmonic atomistic Green’s function for three-dimensional interfaces,” *Phys Rev B* 101(4), 41301 (2020).
- ⁴⁸ T. Feng, Y. Zhong, J. Shi, and X. Ruan, “Unexpected high inelastic phonon transport across solid-solid interface: Modal nonequilibrium molecular dynamics simulations and Landauer analysis,” *Phys Rev B* 99(4), 045301 (2019).
- ⁴⁹ P.K. Schelling, S.R. Phillpot, and P. Keblinski, “Kapitza conductance and phonon scattering at grain boundaries by simulation,” *J Appl Phys* 95(11), 6082–6091 (2004).
- ⁵⁰ J. Shi, J. Lee, Y. Dong, A. Roy, T.S. Fisher, and X. Ruan, “Dominant phonon polarization conversion across dimensionally mismatched interfaces: Carbon-nanotube–graphene junction,” *Phys Rev B* 97(13), 134309 (2018).
- ⁵¹ N.A. Roberts, and D.G. Walker, “Phonon wave-packet simulations of Ar/Kr interfaces for thermal rectification,” *J Appl Phys* 108(12), 123515 (2010).
- ⁵² C.H. Baker, D.A. Jordan, and P.M. Norris, “Application of the wavelet transform to nanoscale thermal transport,” *Phys Rev B* 86(10), 104306 (2012).
- ⁵³ P.K. Schelling, S.R. Phillpot, and P. Keblinski, “Phonon wave-packet dynamics at semiconductor interfaces by molecular-dynamics simulation,” *Appl Phys Lett* 80(14), 2484 (2002).
- ⁵⁴ Y. Chalopin, and S. Volz, “A microscopic formulation of the phonon transmission at the nanoscale,” *Appl Phys Lett* 103(5), 051602 (2013).
- ⁵⁵ K. Sääskilahti, J. Oksanen, J. Tulkki, and S. Volz, “Role of inelastic phonon scattering in the spectrally decomposed thermal conductance at interfaces,” *Phys Rev B* 90(13), 134312 (2014).
- ⁵⁶ K. Sääskilahti, J. Oksanen, J. Tulkki, and S. Volz, “Spectral mapping of heat transfer mechanisms at liquid-solid interfaces,” *Phys Rev E* 93(5), 052141 (2016).

- ⁵⁷ Y. Zhou, and M. Hu, “Full quantification of frequency-dependent interfacial thermal conductance contributed by two- and three-phonon scattering processes from nonequilibrium molecular dynamics simulations,” *Phys Rev B Condens Matter Mater Phys* 95(11), 115313 (2017).
- ⁵⁸ T. Murakami, T. Hori, T. Shiga, and J. Shiomi, “Probing and tuning inelastic phonon conductance across finite-thickness interface,” *Applied Physics Express* 7(12), 121801 (2014).
- ⁵⁹ A. Giri, J.L. Braun, and P.E. Hopkins, “Implications of interfacial bond strength on the spectral contributions to thermal boundary conductance across solid, liquid, and gas interfaces: A molecular dynamics study,” *Journal of Physical Chemistry C* 120(43), 24847–24856 (2016).
- ⁶⁰ K. Gordiz, and A. Henry, “A formalism for calculating the modal contributions to thermal interface conductance,” *New J Phys* 17(10), 103002 (2015).
- ⁶¹ K. Gordiz, and A. Henry, “Phonon transport at interfaces: Determining the correct modes of vibration,” *J Appl Phys* 119(1), 015101 (2016).
- ⁶² K. Gordiz, and A. Henry, “Phonon Transport at Crystalline Si/Ge Interfaces: The Role of Interfacial Modes of Vibration,” *Sci Rep* 6, 23139 (2016).
- ⁶³ P. Reddy, K. Castelino, and A. Majumdar, “Diffuse mismatch model of thermal boundary conductance using exact phonon dispersion,” *Appl Phys Lett* 87(21), 1–3 (2005).
- ⁶⁴ G. Kresse, and J. Furthmüller, “Efficiency of ab-initio total energy calculations for metals and semiconductors using a plane-wave basis set,” *Comput Mater Sci* 6(1), 15–50 (1996).
- ⁶⁵ G. Kresse, and D. Joubert, “From ultrasoft pseudopotentials to the projector augmented-wave method,” *Phys Rev B* 59(3), 1758 (1999).
- ⁶⁶ P.E. Blöchl, “Projector augmented-wave method,” *Phys Rev B* 50(24), 17953 (1994).
- ⁶⁷ P.E. Blöchl, “Projector augmented-wave method,” *Phys Rev B* 50(24), 17953 (1994).
- ⁶⁸ M.J. Waters, J.M. Rondinelli, I.S. Novikov, K. Gubaev, E. V Podryabinkin, and A. V Shapeev, “The MLIP package: moment tensor potentials with MPI and active learning,” *Mach Learn Sci Technol* 2(2), 025002 (2020).
- ⁶⁹ S. Plimpton, “Fast Parallel Algorithms for Short-Range Molecular Dynamics,” Other Information: PBD: May 1993, (1993).
- ⁷⁰ Y. Hu, T. Feng, X. Gu, Z. Fan, X. Wang, M. Lundstrom, S.S. Shrestha, and H. Bao, “Unification of nonequilibrium molecular dynamics and the mode-resolved phonon Boltzmann equation for thermal transport simulations,” *Phys Rev B* 101(15), 155308 (2020).
- ⁷¹ M.J. Fang, C.W. Tsao, and Y.J. Hsu, “Semiconductor nanoheterostructures for photoconversion applications,” *J Phys D Appl Phys* 53(14), 143001 (2020).
- ⁷² B. Radisavljevic, A. Radenovic, J. Brivio, V. Giacometti, and A. Kis, “Single-layer MoS₂ transistors,” *Nature Nanotechnology* 2011 6:3 6(3), 147–150 (2011).

- ⁷³ C. Qiu, Z. Zhang, M. Xiao, Y. Yang, D. Zhong, and L.M. Peng, “Scaling carbon nanotube complementary transistors to 5-nm gate lengths,” *Science* (1979) 355(6322), 271–276 (2017).
- ⁷⁴ A.D. Franklin, and Z. Chen, “Length scaling of carbon nanotube transistors,” *Nature Nanotechnology* 2010 5:12 5(12), 858–862 (2010).
- ⁷⁵ B. Xu, S. Hu, S.W. Hung, C. Shao, H. Chandra, F.R. Chen, T. Kodama, and J. Shiomi, “Weaker bonding can give larger thermal conductance at highly mismatched interfaces,” *Sci Adv* 7(17), 8197–8220 (2021).
- ⁷⁶ M. Masuduzzaman, and B. Kim, “Scale Effects in Nanoscale Heat Transfer for Fourier’s Law in a Dissimilar Molecular Interface,” *ACS Omega* 5(41), 26527–26536 (2020).
- ⁷⁷ Z. Cheng, R. Li, X. Yan, G. Jernigan, J. Shi, M.E. Liao, N.J. Hines, C.A. Gadre, J.C. Idrobo, E. Lee, K.D. Hobart, M.S. Goorsky, X. Pan, T. Luo, and S. Graham, “Experimental observation of localized interfacial phonon modes,” *Nature Communications* 2021 12:1 12(1), 1–10 (2021).
- ⁷⁸ K.C. Collins, S. Chen, and G. Chen, “Effects of surface chemistry on thermal conductance at aluminum-diamond interfaces,” *Appl Phys Lett* 97(8), 83102 (2010).
- ⁷⁹ C. Monachon, and L. Weber, “Thermal boundary conductance of transition metals on diamond,” <https://doi.org/10.1680/Emr.11.00011> 1(2), 89–98 (2015).
- ⁸⁰ T. Feng, Y. Zhong, J. Shi, and X. Ruan, “Unexpected high inelastic phonon transport across solid-solid interface: Modal nonequilibrium molecular dynamics simulations and Landauer analysis,” *Phys Rev B* 99(4), 045301 (2019).
- ⁸¹ R. Xie, J. Tiwari, and T. Feng, “Impacts of various interfacial nanostructures on spectral phonon thermal boundary conductance,” *J Appl Phys* 132(11), 115108 (2022).
- ⁸² V. Sinha, J.J. Gengler, C. Muratore, and J.E. Spowart, “Effects of disorder state and interfacial layer on thermal transport in copper/diamond system,” *J Appl Phys* 117(7), 74305 (2015).
- ⁸³ X. Liu, F. Sun, L. Wang, Z. Wu, X. Wang, J. Wang, M.J. Kim, and H. Zhang, “The role of Cr interlayer in determining interfacial thermal conductance between Cu and diamond,” *Appl Surf Sci* 515, 146046 (2020).
- ⁸⁴ G. Chang, F. Sun, L. Wang, Y. Zhang, X. Wang, J. Wang, M.J. Kim, and H. Zhang, “Mo-interlayer-mediated thermal conductance at Cu/diamond interface measured by time-domain thermoreflectance,” *Compos Part A Appl Sci Manuf* 135, 105921 (2020).
- ⁸⁵ C. Monachon, and L. Weber, “Thermal boundary conductance of transition metals on diamond,” *Emerging Materials Research* 1(2), 89–98 (2012).
- ⁸⁶ E.T. Swartz, and R.O. Pohl, “Thermal boundary resistance,” (n.d.).
- ⁸⁷ H. Subramanyan, K. Kim, T. Lu, J. Zhou, and J. Liu, “On the importance of using exact full phonon dispersions for predicting interfacial thermal conductance of layered materials using diffuse mismatch model,” *AIP Adv* 9(11), 115116 (2019).

⁸⁸ J. Zhou, B. Liao, G. Chen, J. Maassen, and M. Lundstrom, “(Invited) The Landauer Approach to Electron and Phonon Transport,” ECS Trans 69(9), 23 (2015).

⁸⁹ T. Feng, Y. Zhong, J. Shi, and X. Ruan, “Unexpected high inelastic phonon transport across solid-solid interface: Modal nonequilibrium molecular dynamics simulations and Landauer analysis,” Phys Rev B 99(4), 045301 (2019).

⁹⁰ A. Giri, P.E. Hopkins, A. Giri, and E. Hopkins, “A Review of Experimental and Computational Advances in Thermal Boundary Conductance and Nanoscale Thermal Transport across Solid Interfaces,” Adv Funct Mater 30(8), 1903857 (2020).